Development Of An RF Transmission Line For Hyperfine Structure Studies At ISOLDE's VITO Beamline

Carolyn A. Chinatti

Abstract

This work presents the design, optimization, and prototyping of a custom RF transmission line for the VITO beamline at ISOLDE, aimed at enabling high-precision hyperfine spectroscopy of exotic nuclei. The transmission line features a rectangular stripline region, a coaxial region, a four-section tapered transition region, and curved Teflon center conductor supports, all optimized to minimize signal reflections by maintaining a target $50\,\Omega$ impedance while maintaining field uniformity. Electromagnetic simulations confirmed acceptable S-parameter and time-domain reflectometry performance, with low reflection coefficients and uniform impedance across the 0–4 GHz frequency range. Field strength simulations demonstrated consistent RF magnetic and electric field distributions across a wide power range of 0.5–100 W, supporting resonance conditions with minimal reflected power for three isotopes of immediate interest: ^{47}K, ^{48}K, and ^{49}K. Prototyping validated the manufacturability of critical components using water-jet cutting and 3D printing. A magnetic shielding study explored passive shielding using Mu-metal and iron but concluded that active shielding or repositioning external magnetic sources may be necessary to meet experimental field thresholds. Overall, this project establishes a validated design methodology for integrated RF structures in beamline environments, with future work focusing on experimental verification and enhanced magnetic noise mitigation.

1 Introduction

The Versatile Ion-polarized Techniques On-line (VITO) beamline is a specialized experimental station at the Isotope Separator On Line DEvice (ISOLDE) facility at CERN. It is designed to deliver and manipulate spin-polarized radioactive ion beams for precision measurements in nuclear and particle physics. VITO enables studies of exotic nuclei, tests of fundamental symmetries in the weak interaction, and high-resolution hyperfine structure spectroscopy.

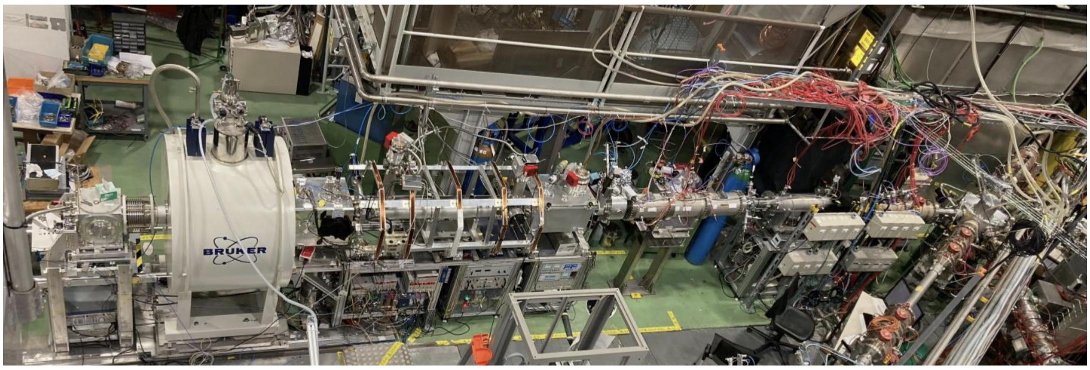

Figure 1: The VITO beamline set up in the ISOLDE experiment room. [1]

This report describes the design and prototyping of a custom radio-frequency (RF) transmission line as part of a planned upgrade to VITO. The objective of the upgrade is to enhance RF delivery for spin-resonance experiments by producing uniform, well-characterized magnetic fields in the interaction region. The project was carried out as part of a technical internship at CERN and consisted of three main components: (i) the electromagnetic design and optimization of the RF line using simulation tools, (ii) the prototyping of the transmission line design, and (iii) the investigation of magnetic shielding to suppress ambient fields along the beam path. The resulting design lays the groundwork for future experiments that require improved control over nuclear spin manipulation.

2 Science Goals of VITO Upgrade

2.1 Hyperfine Structure

Atoms consist of a nucleus surrounded by electrons, both of which possess intrinsic magnetic moments. The interaction between the nuclear and electronic magnetic moments gives rise to a small splitting of atomic energy levels, known as the hyperfine structure as seen in Figure 2. The upgrade to the VITO beamline aims to measure this hyperfine structure in isotopes like ^{47}K, ^{48}K, and ^{49}K.

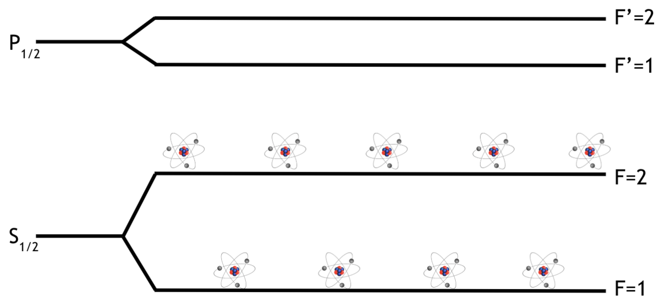

Figure 2: Splitting of energy levels which is known as hyperfine structure. Atoms will be distributed between these two hyperfine levels with some probability determined by the magnetic moments of the nucleus and the electrons.

2.2 Using VITO For Hyperfine Structure Studies

At ISOLDE, radioactive nuclei are produced by bombarding thick targets with high-energy protons from the CERN Proton Synchrotron Booster. These interactions, primarily spallation, fission, or fragmentation, generate a wide range of isotopes. The reaction products diffuse out of the hot target material and are ionized via surface ionization, plasma ionization, or resonant laser ionization. The resulting ions are extracted, accelerated, and mass-separated to isolate the isotope of interest before being delivered to the VITO beamline.

To polarize nuclear spins, the ion beam is neutralized in a charge-exchange cell filled with alkali metal vapor, such as sodium or potassium. This process converts the ions into neutral atoms while preserving their kinetic energy.

Laser spectroscopy will then be employed at VITO to resolve the hyperfine structure. Prior to experimentation, atoms will be distributed between hyperfine levels with some probability determined by the magnetic moments of the nucleus and electrons. In the first step of the experiment, the atomic population is prepared in a single hyperfine level using optical pumping. A laser tuned to a specific hyperfine transition excites atoms in the so-called "visible" level, while atoms in other ("dark") level remain unaffected. Through repeated absorption and spontaneous decay cycles, atoms accumulate in the dark level, effectively polarizing the sample.

An oscillating RF magnetic field will then be applied. For each RF frequency, atoms are transferred back to the visible state with some probability determined by the separation of the hyperfine levels. This transition probability is described by the Rabi formula:

$$P(\Delta, t) = \frac{\Omega_r^2 \sin^2\left(\frac{t}{2}\sqrt{\Omega_r^2 + \Delta^2}\right)}{\Omega_r^2 + \Delta^2}. \tag{1}$$

where Δ is the detuning between the RF frequency and the atomic transition frequency, and Ω_r is the Rabi frequency, proportional to the magnetic field amplitude and transition dipole moment.

Following RF excitation, the laser is reapplied. Atoms returned to the visible state absorb the laser light, become re-excited, and subsequently decay, emitting photons. The number of detected photons is proportional to the population that underwent RF-induced transitions.

By comparing the peak of the number of detected photons to theoretical predictions from the Rabi formula, precision measurements of hyperfine structure constants can be performed. An example of these theoretical predictions can be seen in Figure 3. This enables detailed studies of nuclear electromagnetic moments and weak interaction effects in exotic nuclei.

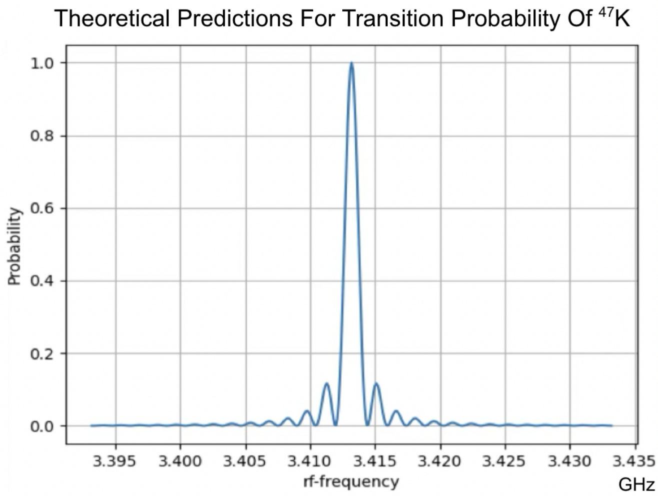

Figure 3: Theoretical predictions for ^{47}K's response to different RF fields. [2]

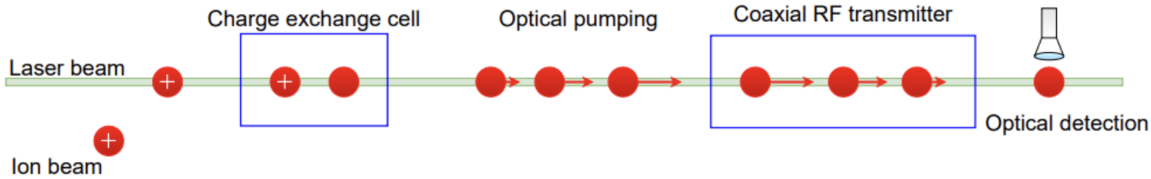

Figure 4: Schematic of the process for studying hyperfine structure in VITO. This project focuses on preparing the RF transmitter region. [3]

A schematic overview of the experimental sequence is shown in Figure 4. The generation of a stable, spatially uniform RF field is essential for high-precision spin manipulation. As such, the forthcoming upgrade to the VITO beamline will integrate a custom-designed RF transmission system optimized for this application.

3 Simulations and Optimization of Transmission Line Design

The goal of this project was to design an RF transmission line capable of delivering precise and efficient RF excitation. Electromagnetic simulations were carried out using CST Studio Suite, a three-dimensional full-wave simulation software. [4]

Although the intended operational frequency range for the final system extends up to 4GHz, most simulations were limited to the 0–2GHz range in order to reduce computational time during the early design phase. Unless otherwise specified, the simulated transmission line was driven with an input power of 0.5W.

Material properties in the simulations were approximated using a Perfect Electric Conductor (PEC) model, which offers idealized conductive behavior. While the final physical prototype will be constructed using aluminum, PEC was employed to simplify calculations and focus on electromagnetic field distribution and impedance characteristics during the optimization process.

3.1 General Geometry Of The Transmission Line

The initial design phase focused on selecting the optimal transmission line geometry. Two configurations were considered: a rectangular stripline and a circular coaxial line. The stripline design would utilize a standard rectangular aluminum waveguide available from the CERN store, with a centrally mounted aluminum signal conductor. The coaxial configuration would consist of two concentric aluminum tubes, also available off the shelf, where the outer tube acts as the ground conductor and the inner tube carries the RF signal. In both cases, the center conductor is connected to an external coaxial cable for power delivery.

In both geometries, the atomic beam passes through the region between the center conductor and the outer conductor, allowing interaction with the RF field.

To determine the optimal configuration, multiple stripline and coaxial designs were modeled in CST. The evaluation focused on magnetic field strength and field uniformity within a 10mm-wide region corresponding to the ion beam path. As shown in Figure 5, the rectangular stripline geometry with a 3mm-thick central conductor provided the most favorable balance between field intensity and homogeneity. This configuration was therefore selected for further development.

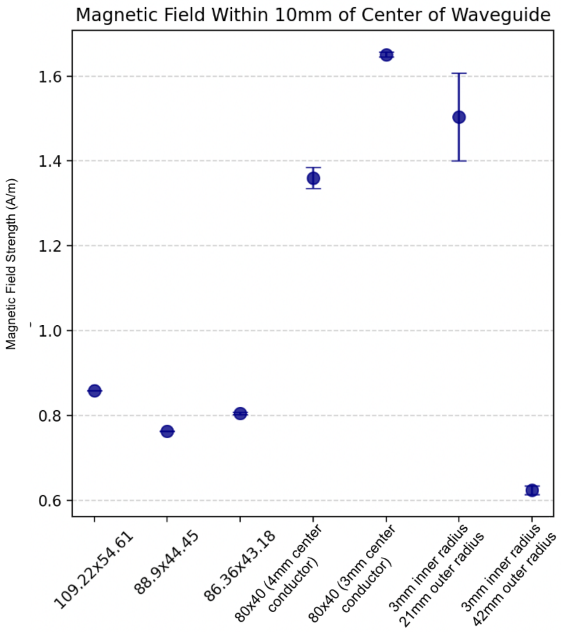

Figure 5: Simulated magnetic field distribution for different transmission line geometries. The points represent the average field strength and the bars show the variation from that average within the ion beam's path. The 80mm x 40mm rectangular stripline with a center conductor with a thickness of 3mm was chosen for its strong, uniform magnetic field.

In addition to field uniformity and impedance matching, cutoff frequencies for each geometry were evaluated to confirm that the 80 mm × 40 mm waveguide was the most suitable option for the transmission line. Since the structure partially resembles a waveguide, it was important to ensure that as much of the operating RF frequency range as possible remained below the cutoff frequency of any higher-order modes that could be supported by the geometry, as these modes could introduce signal distortions.

For each geometry, the cutoff frequency was also calculated in CST. The results are shown in Table 1. Though all are below the optimal value of 4 GHz, the 80 mm × 40 mm waveguide offers the highest cutoff frequency, confirming it as the optimal choice for the line.

Dimensions (mm)	109.22x54.61	88.9x44.5	86.36x43.18	80x40	21 by 3	42 by 3
Cutoff Frequency (GHz)	1.48	1.85	1.91	2.08	1.27	1.70

Table 1: Cutoff frequencies for the different transmission line geometries investigated.

3.2 Initial Impedance Matching

Because the final system incorporates both stripline and coaxial segments, impedance matching between them is essential to minimize signal reflections. To ensure consistent 50Ω impedance throughout the structure, the dimensions of both regions were systematically optimized. A parametric sweep of stripline center conductor widths and coaxial inner conductor radii was performed. As shown in Figure 6, the optimal dimensions were found to be a 34.25mm-wide center conductor for the stripline and a 0.79mm radius inner conductor for the coaxial section.

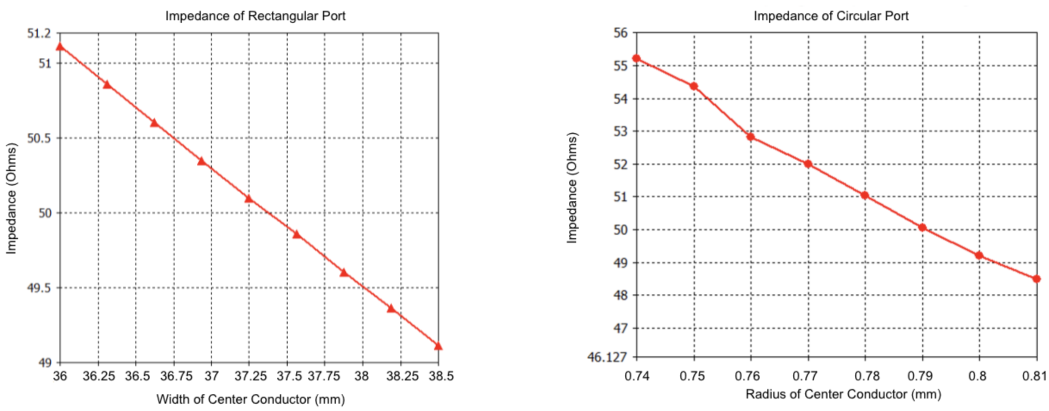

Figure 6: Simulated impedance as a function of stripline width and coaxial conductor radius. The optimal impedance match of 50Ω was achieved using a 34.25mm wide stripline center conductor and a 0.79mm radius coaxial center conductor.

3.3 Transition Region Design

Although both the stripline and coaxial segments were individually impedance-matched to 50Ω, the junction between the rectangular center conductor and the coaxial power input required an optimized transition region. This interface presented a potential source of impedance discontinuity, making the transition geometry critical to maintaining signal integrity and minimizing reflections.

The design was further complicated by the proximity of the transition region to circular apertures required for the atomic beam path, as illustrated in Figure 9b. These geometric constraints precluded simplifications and necessitated detailed three-dimensional modeling.

A variety of transition profiles were investigated as shown in Figure 7, including linear tapers, curved transitions, and segmented tapers.

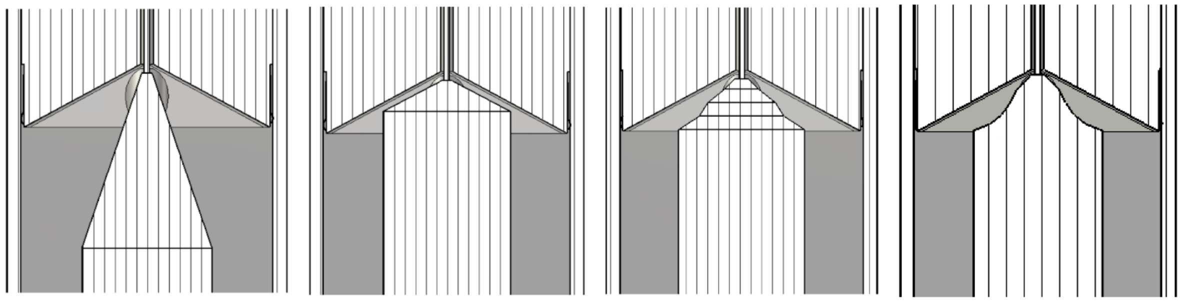

Figure 7: Overview of transition region geometries evaluated during optimization. Variants include linear tapers (angle and length varied), curved transitions (radius and length varied), and segmented tapers (step widths and lengths varied) to minimize impedance mismatch.

Two primary methods were used to evaluate the impedance matching performance of each design:

- **Scattering parameters (S-Parameters)**: These are a set of metrics used to characterize how RF signals behave in a network, particularly in terms of reflection and transmission. In this project, S-parameters were utilized to assess the performance of the transmission line, with a primary focus on S_{11}, or the input reflection coefficient. The S_{11}s in this report are given in the linear scale and therefore indicate the square root of the proportion of the input signal that is sent into one side of the transmission line and then reflected back due to impedance mismatches along the line. Minimizing S_{11} throughout the frequency range was crucial to ensure maximum power transfer and reduce signal loss, thus improving the overall efficiency of the transmission line design.

- **Time Domain Reflectometry (TDR)**: This technique involves injecting a fast-rising voltage pulse into the transmission line and observing the reflected signals over time to identify discontinuities or impedance mismatches. Reflections occur when there is a change in impedance along the line, and the magnitude and timing of these reflections provide information about the location and severity of the mismatch. In this project, TDR was used as a diagnostic tool to evaluate the impedance uniformity of the transmission line. The primary objective was to minimize the amplitude of these reflections, indicating a well-matched line.

Over 100 transition region geometries were simulated by systematically varying including taper length and angle, curvature radius, and segment dimensions, and their influence on impedance continuity and overall RF performance were evaluated using these methods. A selection of representative results for S_{11} and TDR analyses are shown in Figure 8. Based on these simulations, a composite four-section taper was selected as the optimal transition design that ensures a smooth impedance transformation between the coaxial and stripline segments and is shown in Figure 9.

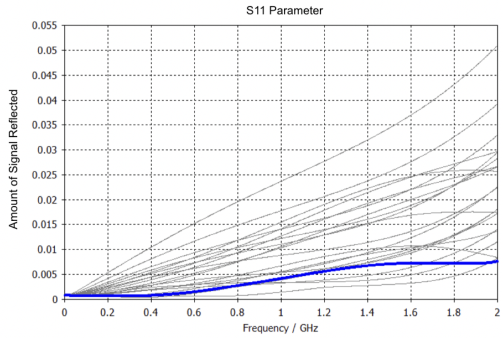

(a)

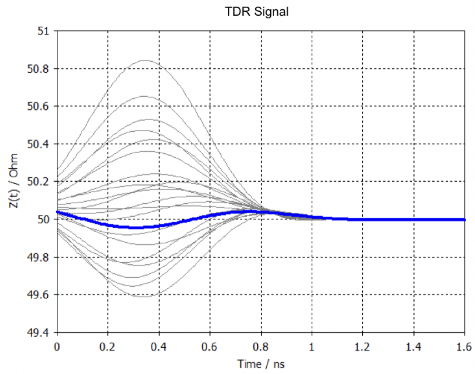

(b)

Figure 8: Simulation results comparing transition region geometries: (a) S_{11} and (b) TDR simulation. The highlighted profile demonstrates the lowest signal reflection and most uniform impedance, confirming it as the optimal transition design.

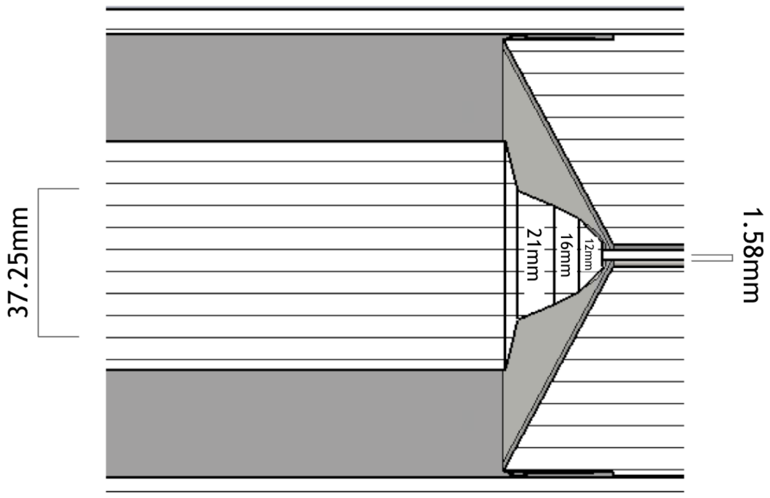

(a) Final transition region composed of four independently optimized taper sections. This configuration minimizes impedance discontinuities, improving signal transmission.

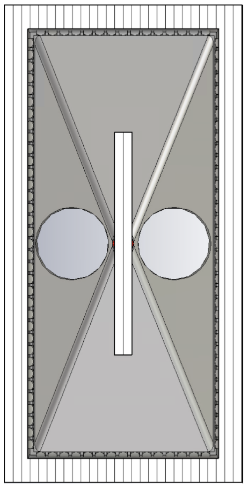

(b) Cross-sectional view of the transition region. The ion beam travels through one of the holes above the center conductor. Although only one beam is used experimentally, previous work demonstrated that symmetrical holes reduce signal reflections. [3]

Figure 9: Views of the transition region. (a) shows the geometry with optimized taper sections; (b) shows a cross-sectional view highlighting the ion beam path.

3.4 Center Conductor Support Design

To ensure mechanical stability of the center conductor within the stripline section, custom Teflon support structures were developed and positioned on both sides of the conductor. Several support configurations were evaluated with the dual objectives of maintaining magnetic field uniformity and minimizing signal reflections. Additionally, the supports had to provide sufficient rigidity while remaining manufacturable using standard workshop tools.

Previous studies demonstrated that continuous supports extending along the entire conductor length offer superior performance compared to segmented or discrete supports [3]. This approach not only enhances mechanical robustness but also minimizes RF field perturbations introduced by discontinuities.

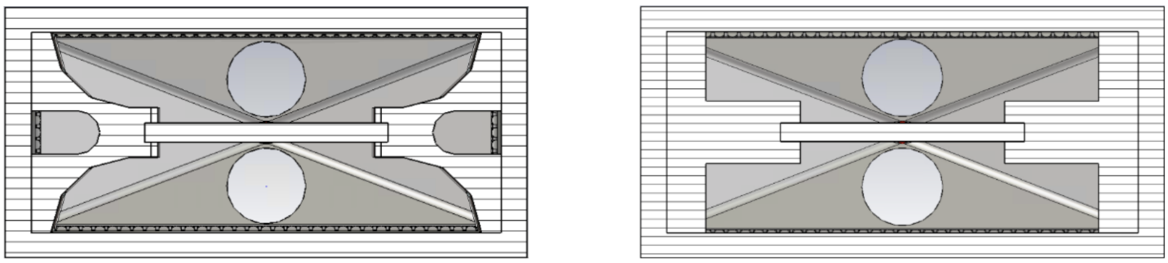

Figure 10: Stripline center conductor support concepts evaluated for mechanical stability and RF compatibility. Investigated designs include curved and block-shaped supports. Additional variants (not shown) involved cutouts and solid-body modifications.

The addition of support structures significantly affected the impedance of the transmission line, resulting in a degradation of S-parameter and TDR performance. Although all support designs introduced some degree of impedance mismatch, the block-shaped support exhibited higher reflection levels compared to the curved support design, as illustrated in Figure 11. Consequently, the curved support geometry was selected for further development and optimization.

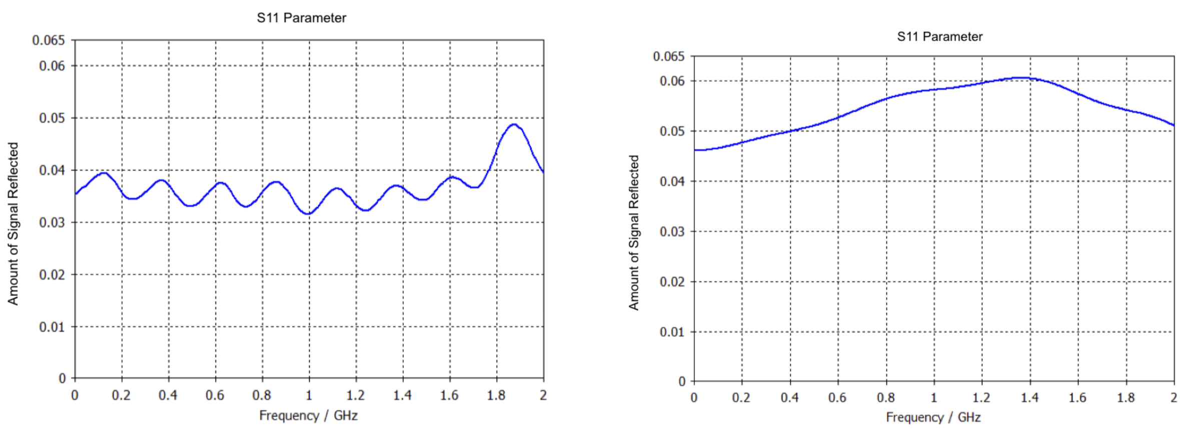

(a) (b)

Figure 11: Simulated S_{11} for a support structure designs incorporating a curved (a) and block (b) Teflon support. The reflected signal amplitude is lower in the curved configuration, indicating improved impedance matching, so it was chosen as the ideal support structure design.

Despite improved performance over the block geometry, the curved supports still introduced a noticeable impedance mismatch due to the dielectric loading effect of the Teflon. This effect was mitigated by narrowing the center conductor by 2mm, thereby compensating for the reduced impedance. The resulting configuration restored the target 50Ω impedance, as confirmed by improved S-parameter and TDR results shown in Figure 12.

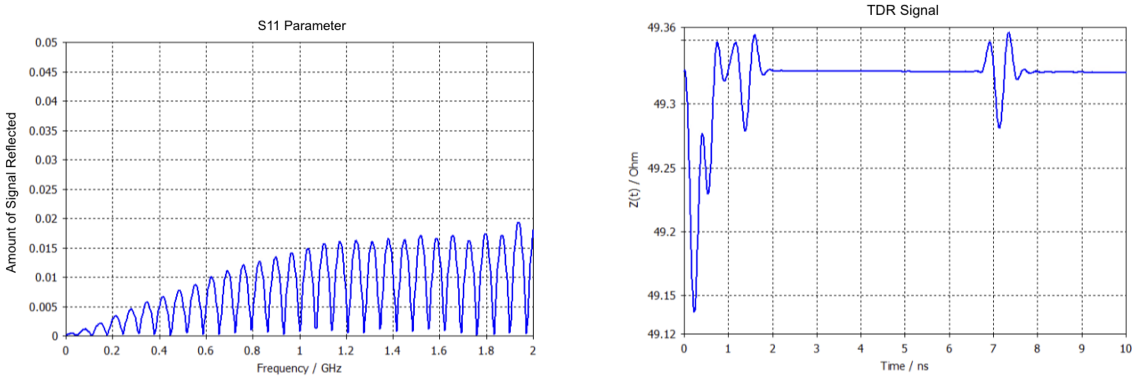

(a) (b)

Figure 12: S_{11} (a) and TDR (b) simulation results after narrowing the center conductor by 2mm in the presence of curved supports. Uniform impedance is re-established, reducing signal reflections.

While the narrowed center conductor slightly reduced RF magnetic field strength and uniformity within the interaction region, the resulting field distribution remained within acceptable limits for experimental requirements, as illustrated in Figures 13 and 14.

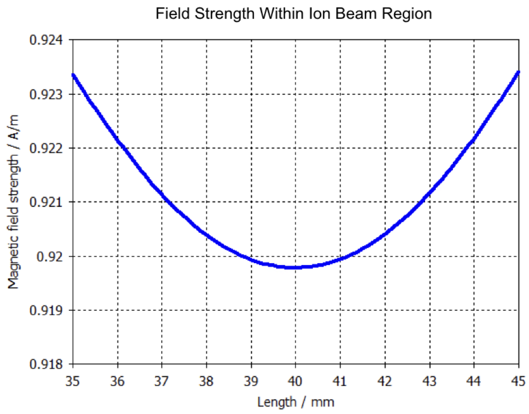

Figure 13: Simulated RF magnetic field strength in the beam interaction region for the final transmission line design. Despite geometric and material additions, the field remains sufficiently strong and uniform.

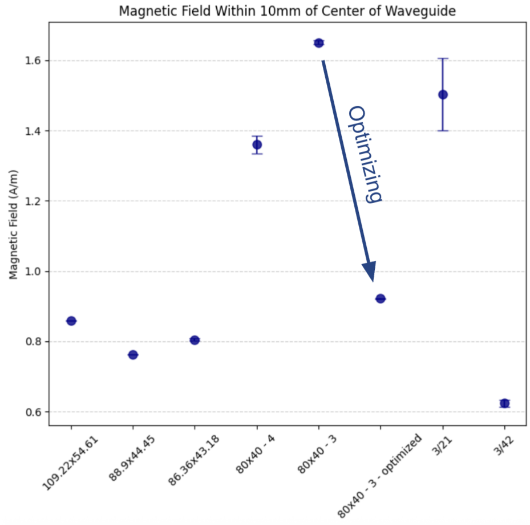

Figure 14: Comparison of RF magnetic field strength and uniformity of the final design compared to other considered geometries. Even after modifications, the final geometry retains a stronger RF field than any other option that provided an acceptably uniform field.

3.5 Final Model and Performance Evaluation

The final transmission line model was assembled incorporating all optimized parameters, including conductor dimensions, transition regions, Teflon supports, and cable interfaces. The design consists of a two-meter-long rectangular stripline, with both the center and outer conductors fabricated from aluminum. Circular-to-rectangular transition regions were added at both ends to connect the stripline to standard coaxial cables, enabling integration with the broader RF system. To improve simulation realism, the conductor material was updated from idealized PEC to aluminum, accounting for ohmic losses and surface conductivity effects.

A high-fidelity simulation was performed with an input power of 0.5W over the full frequency range of 0–4GHz. The resulting S-parameter and TDR plots, shown in Figures 15 and 16, confirm a high degree of impedance matching and minimal signal reflection across the operating band. A contour plot of the resulting magnetic field in a region of the transmission line is shown in Figure 17

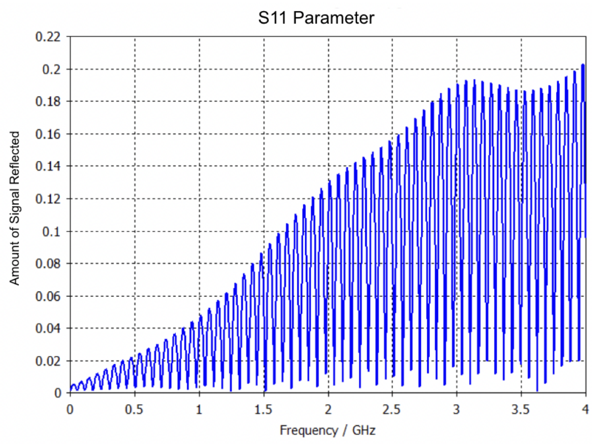

Figure 15: Final S-parameter simulation for the complete transmission line model from 0 to 4GHz. Low S_{11} values across the band confirm a high degree of impedance matching and subsequent minimal signal reflection.

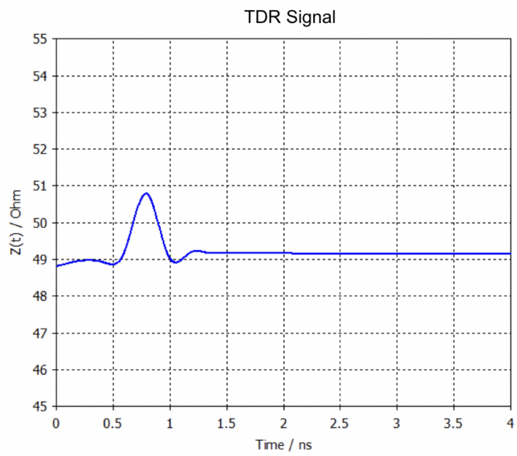

Figure 16: Final TDR plot of the optimized transmission line model. The flat impedance profile indicates excellent uniformity along the line with negligible mismatches.

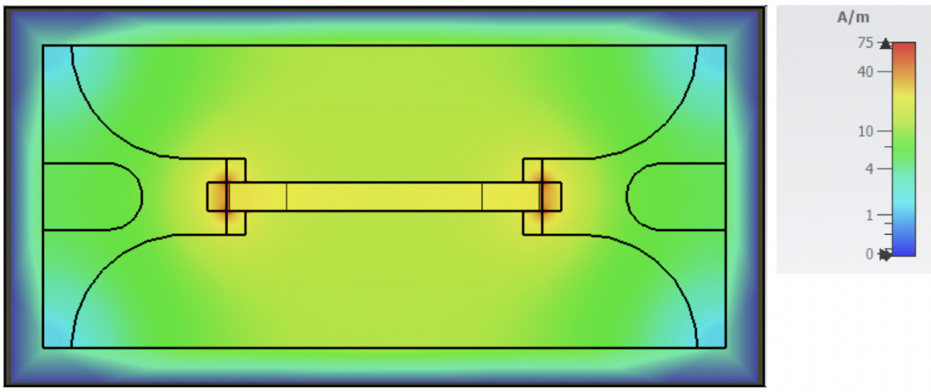

Figure 17: A contour plot of the averaged magnetic field across a slice of the transmission line.

The line's performance under varying input power levels was also evaluated to ensure consistent behavior under elevated power conditions. Simulations were conducted at input powers of 1W, 10W, 30W, 50W, 80W, and 100W. The resulting RF magnetic and electric field strengths within the beam interaction region were found to scale fairly predictably with input power, while field uniformity remained stable. These results, shown in Figure 18, validate the design's robustness across the full operational range.

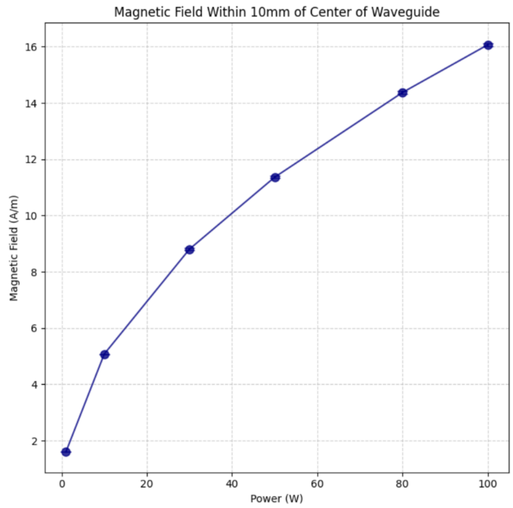

(a)

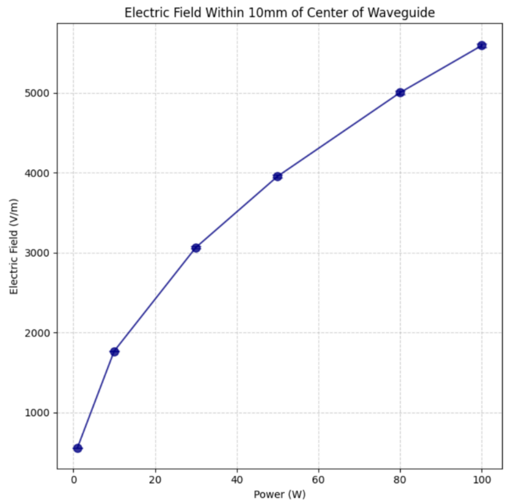

(b)

Figure 18: Field strength and deviation of the electric (a) and magnetic (b) field generated along the beam's path in the transmission line as a function of inputted power. In both cases, performance remains consistent and predictable across a wide power range.

3.6 Input Power Investigation For Isotopes Of Interest

After validating the performance of the transmission line across the full range of operating frequencies, further analysis focused on operating conditions corresponding to the theoretical hyperfine level separations of the potassium isotopes ^{47}K, ^{48}K, and ^{49}K. Particular attention was given to determining the minimum input power required to generate an RF magnetic field of sufficient strength to drive the magnetic dipole hyperfine transitions in each isotope. For ^{48}K, which has a nuclear spin of $I = 1$, two allowed magnetic dipole transitions exist, necessitating investigation of two distinct RF resonance frequencies [5].

To determine the required input power, previous calculations of the magnetic field strength (B_1) necessary for efficient spin excitation at each isotope's resonance frequency (f_{rf}) were used. [2] [6] The high-resolution simulation of the transmission line was then used to extract the RF magnetic field amplitude (B_1^{sim}) produced at a known reference input power (P_{ref}) of 0.5W. Assuming a square root dependence between input power and magnetic field strength in the regime of interest (which is verified in Figure 18), the required input power P_{req} was calculated as

$$P_{\text{req}} = P_{\text{ref}} \left(\frac{B_1}{B_1^{\text{sim}}} \right)^2 . \quad (2)$$

This approach was applied to both the time-averaged and non-averaged magnetic field along the path the beam will follow through the transmission line to provide conservative and idealized estimates, respectively.

The amount of the necessary power that was reflected was also calculated by accounting for the S_{11} at each frequency. The reflected power was therefore determined using

$$P_{\text{reflected}} = P_{\text{req}} * |S_{11}|^2 . \quad (3)$$

The final results are summarized in Tables 2 and 3.

Parameter	^{47}K	^{48}K (Transition 1)	^{48}K (Transition 2)	^{49}K
B_1 (µT)	11.43	9.81	16.96	11.2
f_{rf} (GHz)	3.4132	1.19385	1.19385	2.3682
B at 0.5 W (µT)	1.05	1.13	1.13	1.12
S_{11} (linear)	0.1308	0.0342	0.0342	0.0824
P_{req} (W)	59.25	37.68	112.63	50.00
$P_{\text{reflected}}$ (W)	1.01	0.044	0.132	0.34

Table 2: Required input power and the values necessary to find it in the time-averaged RF field

Parameter	^{47}K	^{48}K (Transition 1)	^{48}K (Transition 2)	^{49}K
B_1 (µT)	11.43	9.81	16.96	11.2
f_{rf} (GHz)	3.4132	1.19385	1.19385	2.3682
B at 0.5 W (µT)	1.48	1.19	1.19	1.52
S_{11} (linear)	0.1308	0.0342	0.0342	0.0824
P_{req} (W)	29.82	33.98	101.56	27.15
$P_{\text{reflected}}$ (W)	0.51	0.040	0.119	0.18

Table 3: Required input power and the values necessary to find it in the non-averaged RF field

The calculated input power requirements for achieving the desired magnetic field strength vary significantly among the isotopes and hyperfine transitions, reflecting differences in resonance frequencies and local field distributions. The power required based on averaged magnetic field values is consistently higher than that derived from non-averaged values, highlighting the importance of considering spatial field variations across the interaction region.

The relatively low S_{11} values across all cases indicate efficient power transfer from the source to the load, with minimal reflection. Nonetheless, even small reflected power levels must be accounted for during system design to ensure optimal excitation efficiency and to protect sensitive components from back-reflected RF energy.

Overall, these results emphasize the importance of accurate magnetic field characterization and careful power budgeting for effective operation of the RF system across different isotopes and transitions.

4 Prototyping

The primary goal of the prototyping phase was to develop and refine an assembly process that enables construction of a physically accurate transmission line model, emphasizing both ease of fabrication and dimensional precision.

The center conductor was fabricated from aluminum via water jet machining to ensure high dimensional accuracy and superior surface finish. Transition region components and internal Teflon support structures were produced using 3D printing, allowing rapid iteration and complex geometries. The outer conductor consisted of an 80mm $\times$ 40mm rectangular aluminum waveguide sourced directly from the CERN store.

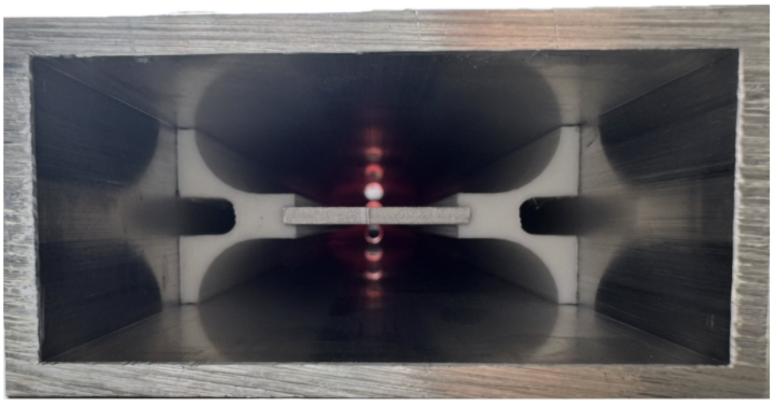

Figure 19: Assembled prototype of the RF transmission line, including water-jet-machined aluminum center conductor, 3D-printed transition regions, and curved Teflon supports housed within an 80mm × 40mm aluminum waveguide.

5 Magnetic Shielding

Magnetic shielding is the process of reducing the influence of external magnetic fields to protect sensitive equipment or processes from magnetic interference. This is typically achieved by enclosing the target region with materials possessing high magnetic permeability, which redirect magnetic flux lines away from critical components. Effective shielding is crucial in systems involving RF fields or other low-level signals, where even weak ambient magnetic disturbances can introduce noise, distortion, or degrade operational precision.

In this project, magnetic shielding was necessary because the transmission line operates in an environment exposed to ambient magnetic fields that could impair system performance and interfere with the precise RF excitation of the ion beam. The experimental requirement mandates maintaining ambient magnetic fields below 3μT within the interaction region.

The first step in the magnetic shielding investigation was to validate CST simulations of the ambient magnetic field along the VITO beamline against experimental measurements. As shown in Figure 20, there is strong agreement between simulated and measured magnetic field magnitudes along the ion beam path, particularly in the Z-component and total field magnitude. Discrepancies observed in the X and Y components are attributed to their comparatively low magnitudes and measurement uncertainties.

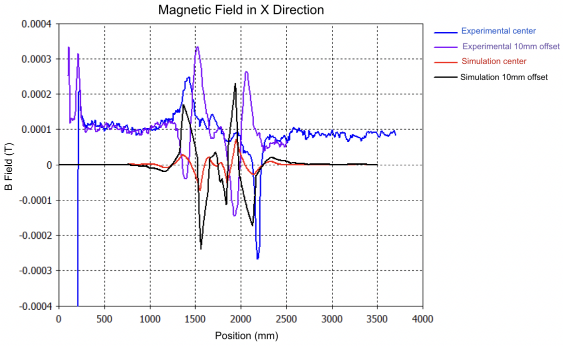

(a)

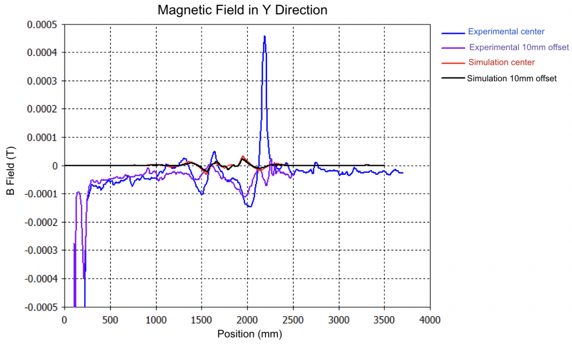

(b)

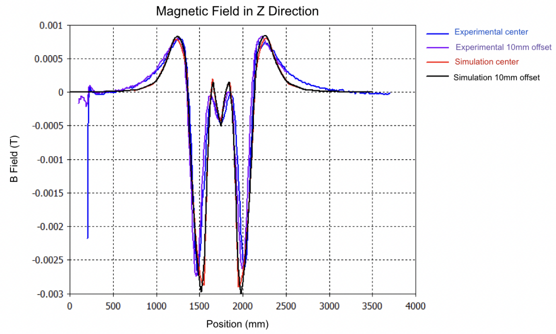

(c)

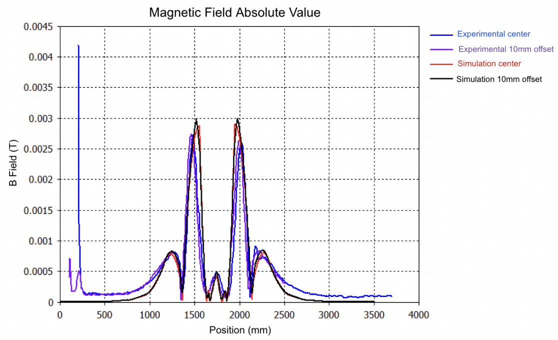

(d)

Figure 20: Comparison between simulated and measured magnetic field components along the ion beam path and along a 1cm offset from the path. (a)–(c) show X, Y, and Z field components, respectively, while (d) shows the absolute field magnitude. The Z-component and total field exhibit strong agreement, validating the simulation. Discrepancies in X and Y are attributed to their lower magnitudes.

Following validation of the ambient field, several magnetic shielding configurations were modeled to reduce the ambient field impacting the ion beam within the transmission line. Shields were simulated using Mu-metal (a high-permeability nickel–iron alloy optimized for magnetic shielding) and iron.

The most effective geometry consisted of a rectangular inner shield enveloped by a circular outer shield. Both shields are designed to be fabricated by folding metal sheets, resulting in regions with overlapping layers, as depicted in Figure 21. The inner shield was composed of Mu-metal, while simulations tested both Mu-metal and iron for the outer shield. The optimal combination was found to be a Mu-metal inner shield paired with an iron outer shield.

However, as shown in Figure 22, even this optimized shield configuration does not achieve the required attenuation to bring the ambient field below the 3μT threshold. Therefore, this investigation concludes that the most effective solution is to remove or reposition the magnets generating the ambient field rather than relying on passive shielding, but active shielding may also prove effective at mitigating the field, so more investigation into this issue will be carried out in the future.

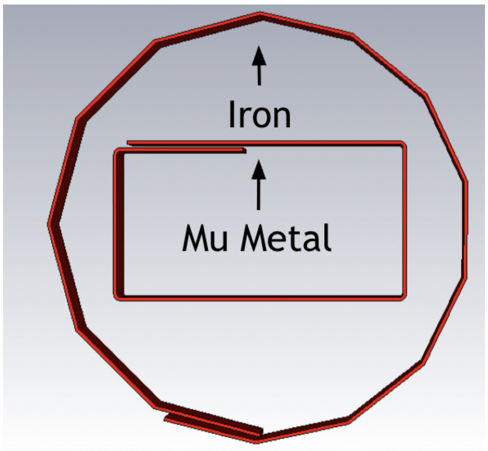

Figure 21: Geometry of the optimized magnetic shielding configuration. The design features a Mu-metal inner shield nested within a folded iron outer shield to maximize field attenuation along the beam path.

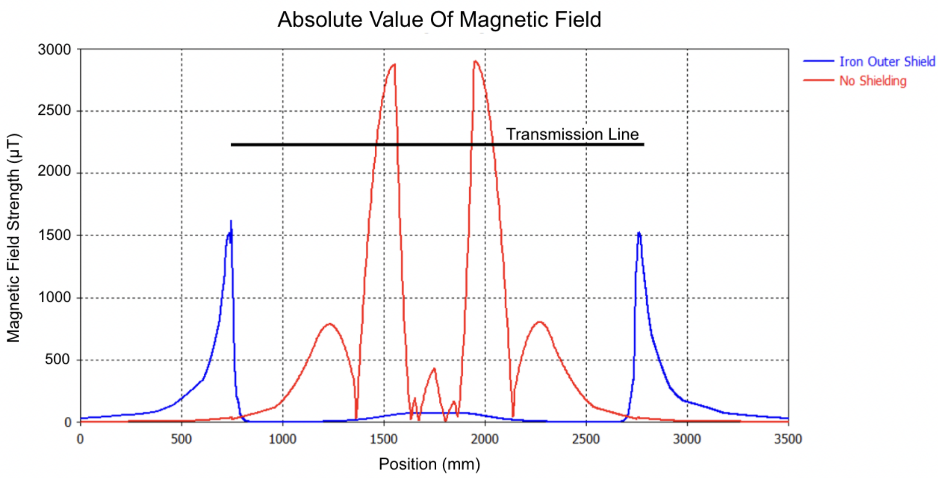

Figure 22: Simulated magnetic field along the beam path with and without the optimal Mu-metal and iron shielding configuration. The black line represents the area the transmission line will sit in. The shielding fails to reduce the field below the experimental threshold of 3μT indicating the need for another method of ambient magnetic field reduction.

6 Conclusion and Future Work

This project successfully developed and optimized a custom RF transmission line tailored for the VITO beamline at ISOLDE, addressing critical challenges in minimizing signal reflections and maintaining uniform RF magnetic fields. By leveraging comprehensive electromagnetic simulations and iterative design refinement, including a novel composite four-section taper and curved Teflon supports, the final design achieves superior impedance matching and mechanical stability while preserving the necessary field uniformity for high-precision ion beam experiments.

The integration of realistic material properties and the prototyping of key components demonstrate the feasibility of transitioning from simulation to physical implementation, providing a robust foundation for future experimental validation.

Looking ahead, the immediate focus will be on detailed experimental characterization of the assembled transmission line using vector network analyzer measurements to verify simulated S-parameters and field uniformity. Insights from these measurements will inform further refinements in geometry and fabrication processes to enhance performance and reliability.

Future work will focus on evaluating active magnetic shielding and exploring the removal or repositioning of nearby magnetic sources.

Moreover, this work establishes a framework for designing advanced RF transmission lines in complex beamline environments, directly supporting improved precision in hyperfine spectroscopy and enabling more detailed studies of exotic nuclear structures at ISOLDE. Future efforts may also explore active magnetic shielding strategies and integration with other beamline components to further mitigate ambient field disturbances and optimize system performance.

References

[1] "VITO Beamline," CERN ISOLDE, Image, accessed August 3, 2025. [Online]. Available: `https://isolde.cern/vito`.

[2] A. Nagpal, *Theoretical and Experimental Studies of Nuclear Electromagnetic Moments*, [PowerPoint slides], CERN, July, 2025.

[3] D. Havránek, *Electronics for Scintillator Detector Readout and Coaxial RF Line for VITO Beamline at ISOLDE Facility at CERN*, Master's thesis, Brno University of Technology, Faculty of Electrical Engineering and Communication, Department of Radio Electronics, 2024. Advised by Mgr. Michael Pešek, Ph.D.

[4] CST Studio Suite, Computer Simulation Technology, Dassault Systèmes, 2025. [Online]. Available: `https://www.3ds.com/products-services/simulia/products/cst-studio-suite/`

[5] K. Kreim, et.al, *Nuclear charge radii of potassium isotopes beyond $N = 28$*, Physics Letters B Volume 731, 4 April 2014, Pages 97-102.

[6] Martin Hove and Roger Silverans, et.al, *Fast Beam Colinear Laser-RF Double Resonances*, Hyperfine Interactions 38, (1987), Pages 773-792.